Geothermics 53 (2015) 385–395

Contents lists available at ScienceDirect

Geothermics

journal homepage: www.elsevier.com/locate/geothermics

The influence of thermal-hydraulic-mechanical- and chemical effects on the evolution of permeability, seismicity and heat production in geothermal reservoirs

Ghazal Izadi[a,b,*], Derek Elsworth[a]

[a] Baker Hughes Inc., Palo Alto, CA 94306, USA
[b] Department of Energy and Mineral Engineering, EMS Energy Institute and G3 Center, Pennsylvania State University, University Park, PA 16802, USA

ARTICLE INFO

Article history:
Received 11 July 2013
Accepted 8 August 2014

Keywords:
Thermal-hydrologic-mechanical-chemical (THMC)
EGS reservoirs
Evolution of permeability
Seismicity
Heat production

ABSTRACT

A coupled continuum model representing thermo-hydro-mechanical behaviors is applied to follow the evolution of induced seismicity within a prototypical enhanced geothermal system (EGS) reservoir. The model is applied to the potential Newberry EGS field (USA) by assuming fracture sizes of 10–1200 m. Models are classified by their conceptualization of the fractured reservoir geometry as networks of discrete fractures and with equivalent fractured media as fill-in. The THMC model is applied to a doublet injector-producer to explore the spatial and temporal triggering of seismicity for varied fracture network geometries both shallow (2000 m) and at depth (2750 m). The magnitude of the resulting seismic events is in the range −2 to +1.9. The largest event size (∼1.9) corresponds to the largest fracture size (∼1200 m) within the reservoir. The rate of hydraulic and thermal transport has a considerable influence on the amount, location, and timing of failure, and ultimately, on the event rate. The event rate is highest when the fracture density is highest (0.9 m^{-1}) and the initial stresses highest (at depth). In all cases, the *a*-value decreases and the *b*-value increases with time. The *b*-value is largest (∼1.34) for the highest fracture density and the highest stress regime. Thermal energy recovered during production is also greatest at depth and for the highest density of fractures.

1. Introduction

In enhanced geothermal systems (EGS), fluid circulation is influenced by thermal-hydro-mechanical effects in the short-term and by chemical reactions in the long-term. These effects may alter fluid transport properties and as a result enhance the permeability of fracture networks (Elsworth, 1989; Goodman, 1976a; Polak et al., 2003; Renshaw, 1995). Natural and induced fractures, as well as the geometry of fracture networks, have an important influence on both the evolution of permeability (Polak et al., 2003; Yeo et al., 1998) and on induced seismicity (Shapiro and Dinske, 2007).

Many field experiments (Audigane et al., 2002; Delépine et al., 2004; Jung et al., 1996; Rutledge and Phillips, 2003; Zoback and Harjes, 1997) and models (Rutqvist et al., 2001; Shapiro et al., 1998, 2002; Taron et al., 2009a) have been used to determine the key factors influencing the principal processes of permeability enhancement and how they will influence induced seismicity by the action of hydraulic or thermal effects at different times (Baisch, 2009; Deichmann and Giardini, 2009; Dinske et al., 2010; Evans et al., 2005; Shapiro and Dinske, 2007; Taron and Elsworth, 2009; Taron et al., 2009a,b; Yasuhara et al., 2004). Simulating these behaviors requires that the linkage between the fluid and thermal behaviors and the role of fracture networks be defined within the reservoir. This work attempts to determine- how such processes will evolve through time.

Circulating fluid at elevated pressures within naturally fractured reservoirs may cause induced seismicity in the early stages of reservoir stimulation (few weeks) (Rothert and Shapiro, 2003; Rutledge and Phillips, 2003; Shapiro et al., 2002). Hydraulic effects observed during the stimulation of EGS reservoirs influence the permeability and dilation of existing fractures by altering the direction and magnitude of the reservoir stress field. Circulating fluid-induced thermal stresses may also enhance reservoir permeability by creating new fractures and by enhancing the permeability of existing fractures. Both of these effects may induce seismicity both during stimulation and later long-term production.

In this work, we apply a THMC flow-transport-deformation simulator to examine the importance of these factors on reservoir evolution and specifically on the strength of their influence. The focus of this study is to observe the evolution of dominant

* Corresponding author. Tel.: +1 814 777 4099.
E-mail address: ghazal.izadi@bakerhughes.com (G. Izadi).

http://dx.doi.org/10.1016/j.geothermics.2014.08.005
0375-6505/

fracture behaviors that lead to enhanced permeability and induced seismicity during the long-term (~20 year) production of thermal energy from engineered geothermal systems (EGS). We also focus on the significant influence of fracture density and fracture spacing on long-term reservoir behavior.

This paper provides a brief description of the fracture network model and mechanisms of shear failure that result from circulating cold injection fluids at modest overpressures and under pressures. Effective stresses, modulated by fluid pressures and thermal stresses, are used to define the spatial and temporal release of seismic energy as individual fractures are reactivated in shear. The progress of fluid pressures and cooling in the reservoir is represented by the advancement of the hydrodynamic and thermal fronts as well as the progress of pore-pressures and thermal stresses within the reservoir. The triggering of seismicity and the frequency–magnitude distribution (*a*- and *b*-values) of this seismicity is indexed to the progress of these fluid and thermal fronts. These behaviors are evaluated for parameters that broadly represent the planned Newberry Volcano EGS demonstration project and follow the anticipated evolution of the seismic event-size distribution due to fluid and thermal effects during long-term stimulation. Finally, and perhaps most importantly, the relative effects of the above mechanisms on the ultimate recovery of thermal energy from the EGS reservoir are evaluated.

2. Reservoir simulation

The simulations presented in the following uses a THMC simulator (Taron and Elsworth, 2009) that couples the multiphase, multicomponent, non-isothermal thermodynamic, reactive transport and chemical precipitation/dissolution capabilities of TOUGHREACT with the stress/deformation analysis by using the numerical modeling code FLAC^{3D}. The model incorporates the effects of fractured reservoirs involving fracture networks of variable densities and connectivities while considering various reservoir conditions, including initial stress, temperature, and permeability – as these may exert significant influence on the evolution of permeability and seismicity.

Brittle failure on pre-existing fractures is represented as a prescribed stress drop (~3 MPa). For a prescribed frictional strength, the model calculates the shear resistance from the change of normal stress and pore pressure. Stress builds and reaches a peak strength, which then rapidly declines to a residual strength (Goodman, 1976b; Jaeger et al., 2007). This model is used to follow the evolution of seismic rupture within the system.

The principal assumption in this procedure is that strength will fully recover in the interseismic period, allowing the failure cycle to repeat once shear stresses have rebuilt. To define the evolution of failure in a stimulated reservoir, the failure of the seeded fractures is calculated within FLAC^{3D}. Strength is determined by comparing the peak strength and residual shear strength, according to the Mohr–Columb criterion (see Table 2).

2.1. Characteristics of the reservoir

This model is now applied to a doublet geometry within a reservoir with half-symmetry (2000 m × 1000 m × 300 m; Fig. 1), representing the Newberry geothermal field. The Newberry demonstration EGS project is located southeast of Bend, Oregon. Data from well NWG 55–29 are used to build the reservoir model used in the subsequent simulation (Cladouhos et al., 2011). This presumed half-symmetry is approximate but represents the essence of important behaviors that act in the reservoir. A single well injects water at a constant temperature with a withdrawal well separated by 700 m. Boundary stresses, in both horizontal and vertical directions, as well as pore pressure and temperature roughly corresponding to depths of 2000 and 2750 are applied to two different realizations of the geometry (Table 2) applied for this geothermal field. The characteristics and the values of the parameters in the simulation for the in situ reservoir are defined in Table 1.

Table 1
Solid medium properties as used in simulations.

Parameter	Unit	Newberry
Bulk modulus of intact rock(K_m)	GPa	17
Cohesion	MPA	10
Poisson's ratio(υ)	–	0.27
Bulk modulus of fluid(k_f)	GPa	8
Bulk modulus of solid grain(K_s)	GPa	54.5
Internal friction angle(φ)	°	35
Residual friction angel(β)	°	11
Coefficient of thermal expansion(α_T)	1/°C	1.2E−5
Thermal conductivity(λ)	W/m K	2.9
Heat capacity(c_p)	J/kg K	918
Initial permeability (k)	m^2	1.10E−17
Porosity within fractures (ϕ)	–	0.3

Table 2
Parameters utilized in the simulation.

Parameters	Unit	Depth (m)	
		2000 Zone B	2750 Zone D
S_{hmin}	MPa	36	50
SH_{max}	MPa	48	64
S_v	MPa	48	66
$P_{injection}$	MPa	29	35
$P_{reservoir}$	MPa	24	30
$P_{production}$	MPa	19	25
Peak strength	MPa	25	35
$T_{reservoir}$	°C	230	290
$T_{injection}$	°C	20	20
Specific heat	kJ/kg K	4.65	5.6

Prior to long-term production, the reservoir is hydraulically stimulated by elevating fluid pressures and quenching the reservoir at the injection well and withdrawal well over a period of 21 days and at an overpressure of 5 MPa (Izadi and Elsworth, 2014). This dilates pre-existing fractures (fracture propagation is not considered) and allows the development of hydroshears. During the short stimulation (~21 days), four zones – at depths 2000, 2500, 2750 and 3000 m – are considered for reservoir stimulation (Izadi and Elsworth, 2014).

During this stimulation a similar evolution of permeability and progress of seismicity is observed for both zones B (shallowest, located at 2000 m depth) and E (deepest, located at 3000 m depth), and for both intermediate zones C and D (due to the similar form of the fracture networks (0.9 m^{-1}) in zones C and D). Thus, in this study, numerical experiments are conducted for the shallow zone B (with 0.5 m^{-1} fracture density) and deep zone D (with 0.9 m^{-1} fracture density), alone, as representative of the reservoir. These represent behavior at two different depths of 2000 m and 2750 m to examine the roles of the critical influencing parameters, viz. fracture geometry and stress. Each of these zones requires different inputs for fracture orientations, density and spacing (Table 3). Available, but sparse, fracture data for the Newberry geothermal field (Cladouhos et al., 2011) are used to build the fracture networks for the models. Following stimulation, cold fluid (20 °C) is circulated within the reservoir in the doublet pattern of Fig. 1. The resulting analyses examine the progress of seismicity for long-term production as the reservoir is developed in terms of rates, magnitudes and locations.

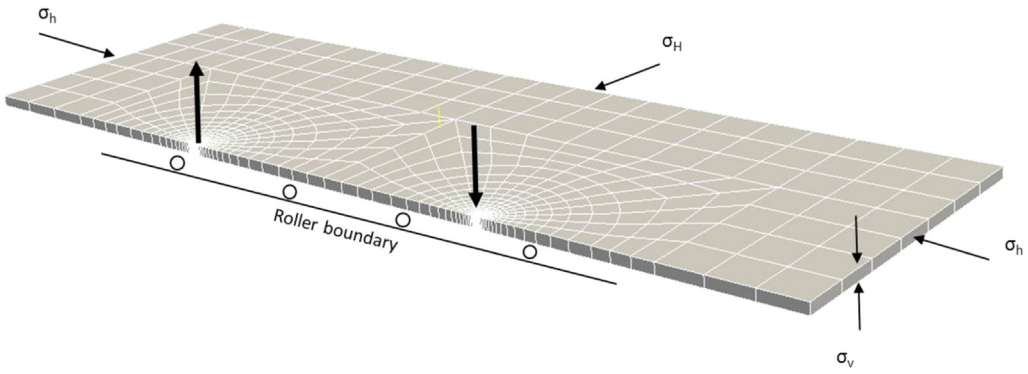

Fig. 1. Geometric layout of EGS reservoir as used in the simulation. Reservoir geometry with half-symmetry (2000 m × 1000 m × 300 m). The spacing between injection and production well is assumed to be 700 m. A vertical and two horizontal stresses are indicated.

Table 3
Fracture data that utilized in the simulation.

Fracture characterization	Unit	Depth (m)	
		2000 Zone B	2750 Zone D
Density	m^{-1}	15/30 m	27/30 m
Number of seeded fractures	–	1000	1800
Fracture size	m	10–1200	10–1200
Fracture spacing	m	10–300	10–300
Standard deviation ($\tilde{\sigma}$)	–	19	19
Mean ($\tilde{\mu}$)	–	360	360

2.2. Characteristics of the fracture network

The presumed fracture orientation and density representing the reservoir are defined in Table 3. The deeper zone D differs from shallower zone B because it has a larger fracture density (0.9 m^{-1} vs. 0.5 m^{-1}) and higher in situ stresses (Table 2) – two features that result in a significantly greater stimulated volume (Izadi and Elsworth, 2014).

Two sets of pre-existing fractures are generated in the reservoir. These comprise a set of long (200–1200 m), widely spaced fractures and a set of short (10–200 m), closely spaced fractures to fill-in between the larger fractures. This allows the fracture network to be generated to honor the BHTV image log data (Cladouhos et al., 2011) (see Fig. 2) for the Newberry reservoir.

The shallow (B) and deep (D) reservoirs have different (low and high) fracture densities. Thus different sets of fracture network models are examined to determine the important influence of the fracture density on response. Both the deeper reservoir (D), with a high density fracture network and shallow reservoir B, with low density, have the same overprinted network of large fractures (density of 0.003 m^{-1} and spacing 300 m) (Fig. 2).

Permeability evolution is calculated from changes of the fracture aperture and the predefined spacing of fractures. Therefore, a sensitivity analysis is conducted to determine the influence of fracture spacing on permeability evolution. A more finely fractured representation of zones B and D (shallow and deep) is developed to examine the effect of a reduced average spacing of the large fractures on rates of seismicity and permeability evolution. Fig. 3 illustrates the geometry of these two networks; the spacing of the large fractures is halved (~150 m) for both zones.

The fracture characteristics listed in Table 3 represent the various fracture densities, orientations and lengths applied in the two zones and are used to examine the response of shallow (B) and deep (D) reservoirs to determine the induced seismicity during long-term (20 years) production.

3. Evolution of shear failure of pre-existing fractures

Shear failure calculations are handled with FLAC^{3D}. In all simulations, the friction angle on fractures is assumed constant (35°). Stress drops resulting from the anticipated fracture networks are shown in Fig. 4 (mean spacing 300 m). Fig. 5 (mean spacing 150 m) shows stress drops for the denser network (halved spacing).

The stress drops along the large fractures are capped at the prescribed stress drop, τ. However, for the larger fracture density (smaller spacing of Fig. 3), the mean stress drop is shown to be smaller than the maximum potential stress drop. This result shows that more closely spaced fractures allow the more rapid removal of heat from the blocks. In such a case failure occurs with a smaller stress drop compared to that for the larger fracture spacing.

A significantly higher rate of fracture reactivations is observed for high density fracture networks (zone D), causing an increase in stress rate compared to the low density fracture network (zone B) Fig. 4. The reason for this is related to the faster propagation (two times faster) of the thermal front by advective transport as well as conductive heat transfer within the higher conductive fracture zones when the density of the fracture network is larger (0.9 m^{-1}) compared to the lower fracture density network (0.5 m^{-1}) in the shallow zone.

Understanding the stress drop distribution is significant for further analysis of the evolution of induced seismicity. Therefore, the following sections illustrate that the highest seismic activity will occur when the stress drop is close to that capped at the prescribed stress drop.

4. Evolution of moment magnitude during production

Next we evaluate the cumulative potential release of energy (Izadi and Elsworth, 2014) from penny shaped fractures of multiple orientations and sizes that are seeded in the reservoir. The potential energy release is a function of the shear stress drop ($\Delta\tau$), the radius of the planar fracture and also the shear modulus (G). Energy release from a pre-existing fracture increases with the square of the stress drop and the cube of the fracture size (Izadi and Elsworth, 2013). It is triggered by the evolving stress state due to pore pressures and induced thermal and chemical strains. Energy release from fractures is most conveniently represented as a moment magnitude (Aki, 1967; Kanamori, 1977; Keylis-Borok, 1959). The moment magnitude relation is defined as (Purcaru and Berckemer, 1978):

$$\log M_0 = 1.5M_s + 9.1 \quad (1)$$

where M_0 is seismic moment and M_S is moment magnitude. In this model, M_0 is the seismic energy derived from the elastic energy released by the shear on pre-existing fractures.

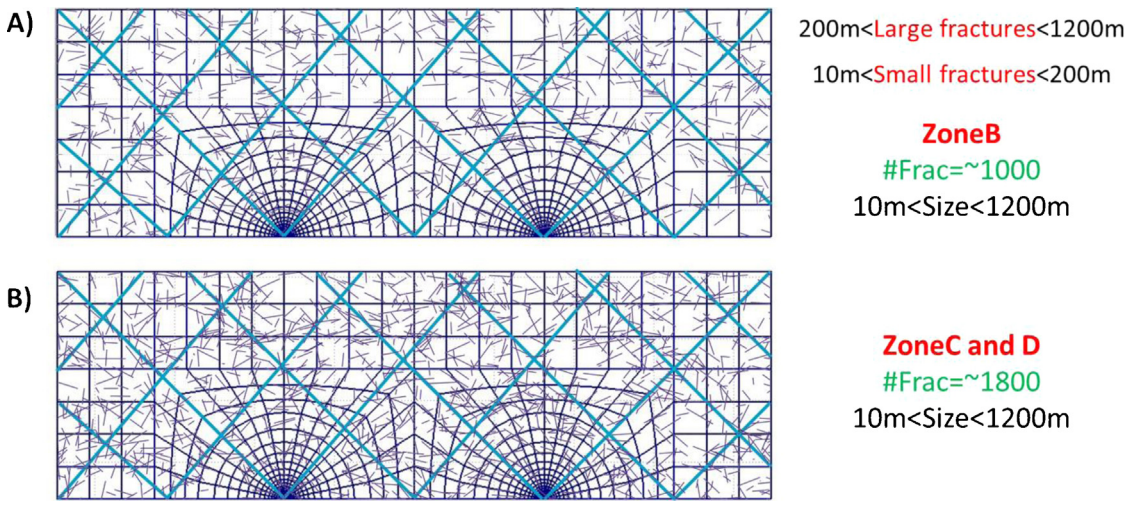

Fig. 2. Fracture network structure for the Newberry EGS reservoir; fracture size varies from 10 m to 1200 m. The same network of large fractures (density of 0.003 m^{-1} and spacing 300 m) is defined for shallow zone B and deep zone D. (A) For smaller fracture (10–200 m) the fracture densities of 0.5 m^{-1} in the shallow zone B. (B) Fracture density of 0.9 m^{-1} applied in the deeper zone D.

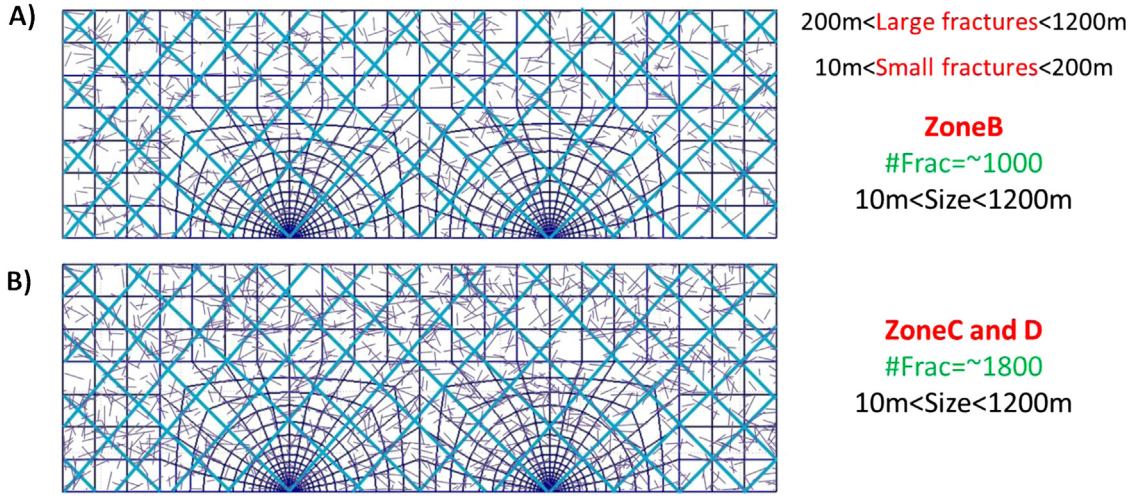

Fig. 3. Fracture network structure for the Newberry EGS reservoir, fracture size varies between 10 m to 1200 m. The same network of large fractures (density of 0.006 m^{-1} and spacing 150 m) defined for shallow zone B and deep zone D. (A) For smaller fracture (10–200 m) the fracture densities of 0.5 m^{-1} in the shallow zone B. (B) Fracture density of 0.9 m^{-1} applied in the deeper zone D.

The spatial/temporal evolution of moment magnitude in the reservoir for the ensemble arrangement of fractures is determined using the above relations. For minimum (10 m) to maximum (1200 m) fracture radii, a maximum shear stress drop of ~3 MPa and a shear modulus of 10 GPa, M_S varies from −2 to +1.9. The largest event size (~1.9) corresponds to the largest fracture size (~1200 m) within the reservoir.

To determine the evolution of moment magnitude during long-term production, we examine the behavior of the two fracture networks models, first shallow and then at depth.

First: the same network of large fractures (density of 0.003 m^{-1} and spacing 300 m) is defined for both the shallow zone (B) and the deep zone (D). However, the smaller fractures (length 10–200 m) are set with a lower fracture density (0.5 m^{-1}) in the shallow zone (B) and a higher fracture density (0.9 m^{-1}) in the deeper zone (D) (Fig. 2). The evolution of moment magnitude for these sets of fracture networks is shown in Fig. 6.

Second: a fractured network (Fig. 3) is developed, representing the two zones (shallow zone B and deep zone D) to examine the effect of a reduced average spacing of the large fractures on the evolution of moment magnitude. Such a fracture network is modeled with both large and small fractures. The fracture density of the larger fractures is ~0.006 m^{-1} with a spacing of 150 m. The smaller fracture set (10–200 m) has a fracture density of 0.5 m^{-1} in the shallow zone B and 0.9 m^{-1} in the deeper zone D. The evolution of moment magnitude for these sets of fracture networks is shown in Fig. 7.

The outcomes for moment magnitude evolution for these different cases allow comparison of the effects of various fracture density, spacing and stress states as a result of reservoir production. During the evolution of energy release, the principal difference between zones B (shallow) and D (deep) for both large (~300 m) and small (~150 m) fracture spacing is related to first, the density of the closely spaced fracture and second, the incremental stress drop that accompanies failure. When the potential energy released in the two zones (shallow to deep) is compared, it is observed that the release begins and builds earlier and reaches further from the injection wellbore for the largest fracture density (0.9 m^{-1}) (Figs. 6B and 7B).

The response for different realizations of fracture network spacing is compared and contrasted for both shallow and deep zones. This analysis is based on small (~150 m) Fig. 7 and large (~300 m) (Fig. 6) fracture spacing for widely-spaced and large fractures in the

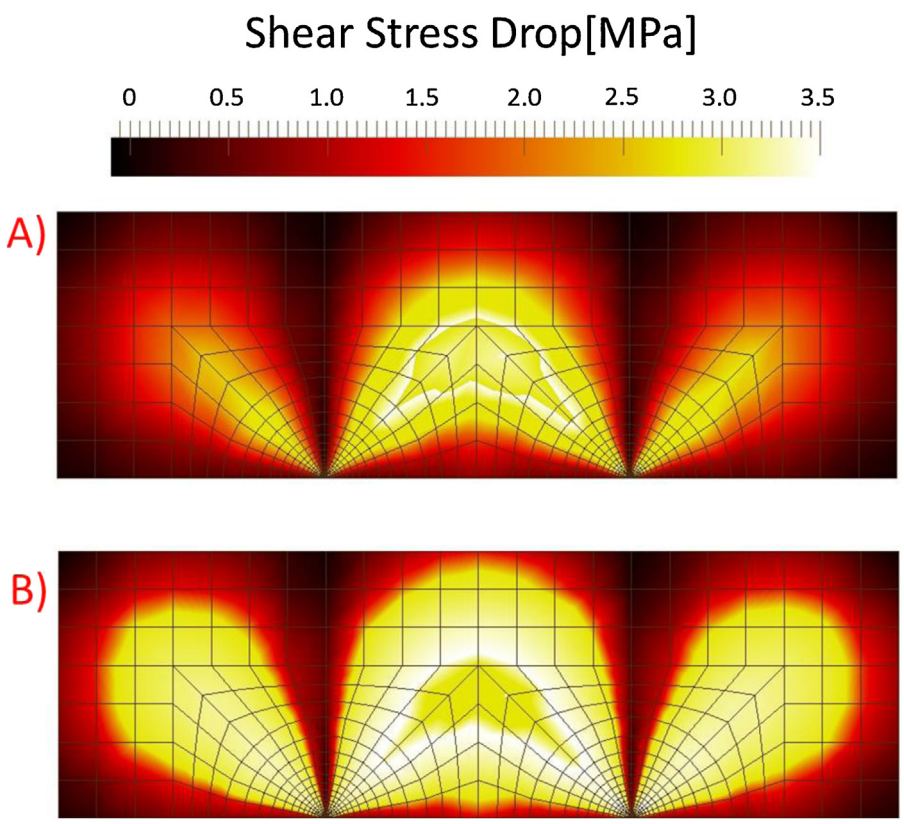

Fig. 4. Development of stress drop at four different zones (shallow to deep) and at four different depths of 2000 and 2750 after 20 years of reservoir production. The same network of large fractures (density of 0.003 m^{-1} and spacing 300 m) applied at each zone. (A) For smaller fracture (10–200 m) the densities of 0.5 m^{-1} in the shallow zone B. (B) Fracture density of 0.9 m^{-1} applied in the deeper zone D.

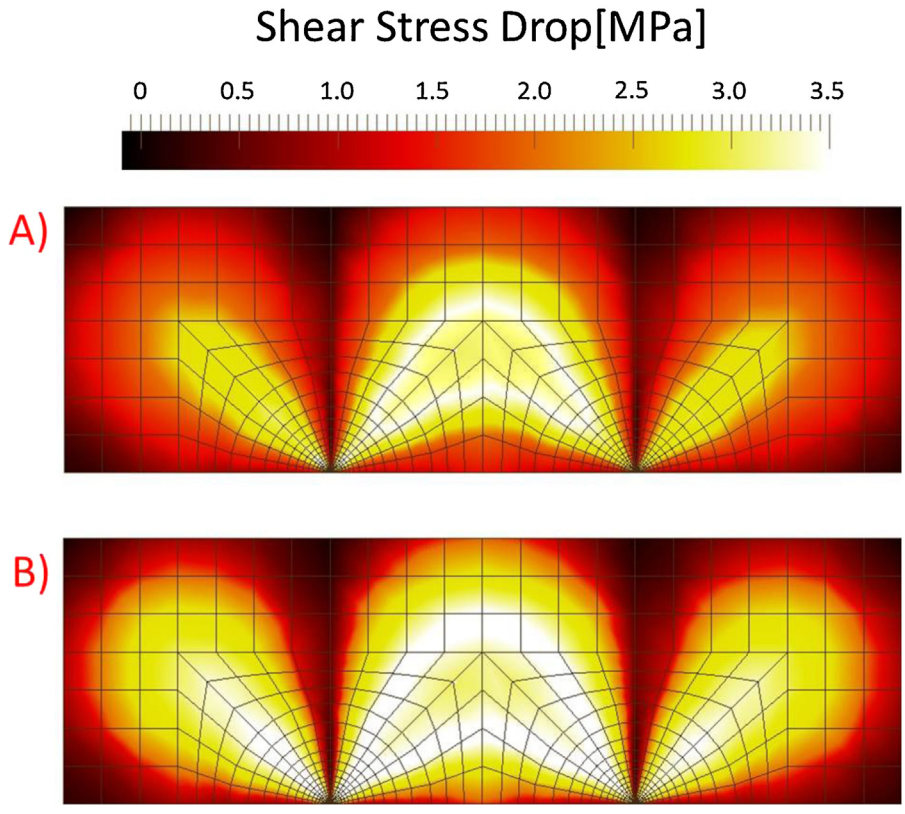

Fig. 5. Development of stress drop at four different zones (shallow to deep) and at four different depths of 2000 and 2750 after 20 years of reservoir production. The same network of large fractures (density of 0.006 m^{-1} and spacing 150 m) applied at each zone. (A) For smaller fracture (10–200 m) the densities of 0.5 m^{-1} in the shallow zone B. (B) Fracture density of 0.9 m^{-1} applied in the deeper zone D.

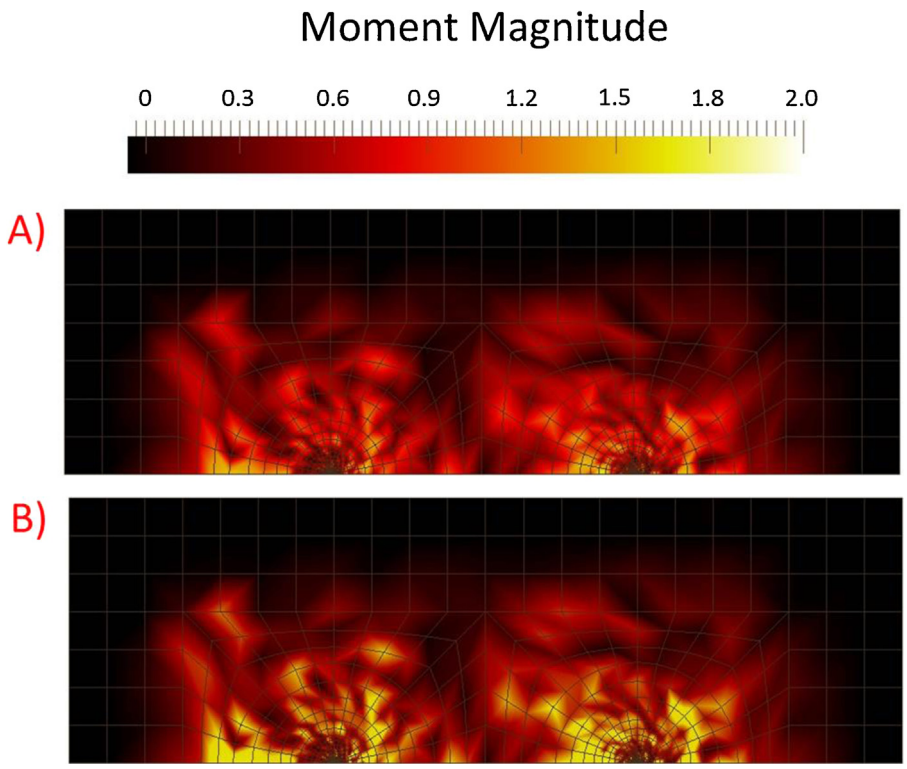

Fig. 6. Evolution of moment magnitude at zones B and D (shallow to deep) and at two different depths of 2000 and 2750 after 20 years of reservoir production. The same network of large fractures (density of 0.003 m^{-1} and spacing 300 m) applied at each zone. (A) For smaller fracture (10–200 m) the densities of 0.5 m^{-1} in the shallow zone B. (B) Fracture density of 0.9 m^{-1} applied in the deeper zone D.

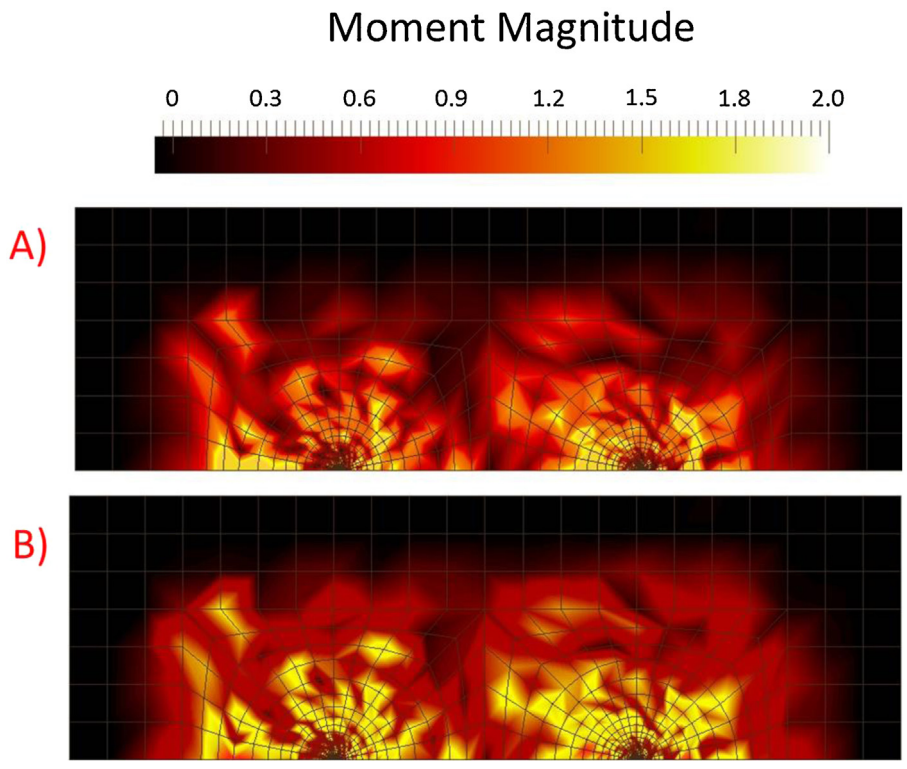

Fig. 7. Evolution of moment magnitude at zones B and D (shallow to deep) and at two different depths of 2000 and 2750 after 20 years of reservoir production. The same network of large fractures (density of 0.006 m^{-1} and spacing 150 m) applied at each zone. (A) For smaller fracture (10–200 m) the densities of 0.5 m^{-1} in the shallow zone B. (B) Fracture density of 0.9 m^{-1} applied in the deeper zone D.

shallow (B) and deep zones (D). The rate of seismic event migration within the reservoir is controlled principally by the density and spacing of the fractures.

The model with the higher fracture density ($0.9\,m^{-1}$) and smaller fracture spacing (150 m) Fig. 7B apparently generates both the greatest number and the largest seismic events ($M_S = 1.9$) after 20 years of reservoir production. Absolute stress is largest when the reservoir is deepest, but stress drop is limited by the difference in peak and residual strength of the fractures (~3 MPa) and hence cannot be a critical parameter. This behavior occurs because transport of fluid pressure and thermal removal from blocks is much faster for the closely spaced fractures (~150 m) than for the network with widely spaced fractures (~300 m). As a result, the fluid propagates faster with distance than for the more closely spaced fractures as observed in Fig. 7B in a given time. The event rate is higher when the fracture network has the larger density ($0.9\,m^{-1}$), with smaller fracture spacing (~150 m), and is located at a depth where the initial stresses are higher (zone D).

4.1. Evolution of seismic events

Using a stress–strain fracture criterion to determine the total strain energy available for release (this energy is assumed to be shed seismically), we observe that during the rupture process the shear stress drops an amount $\Delta\tau$ from an initial value of τ_i to a final value τ_f. The total energy is calculated from the strain changes and volume of the matrix (Izadi and Elsworth, 2013). A relation is introduced to determine the number of events which occur during the failure process based on potential and total energy as

$$N_{event} = \frac{E_T}{E_p} \tag{2}$$

where N_{event} is the number of seismic events, E_T is the total energy and E_p is the potential energy. The model introduced above allows the prediction of the number of seismic events during long-term stimulation. The release of seismic energy, which is generated in the proposed Newberry EGS reservoir due to thermal, hydraulic and mechanical effects, is calculated for shallow ($0.5\,m^{-1}$) to deep zones ($0.9\,m^{-1}$) for small (~150 m) to large (~300 m) fracture spacing. These outcomes allow a comparison of the effects of the low and high fracture densities as well as small and large fracture spacing.

The characteristic event magnitude distribution that occurs in such cases is defined based on the size, population, location, and spacing of larger fractures (200–1200 m). Results indicate that a higher density fracture network ($0.9\,m^{-1}$) with small fracture spacing (~150 m) experiences significantly increased rates of event migration and is associated with a higher number of seismic events compared to those with larger fracture spacing (300 m).

The largest events appear to occur close to existing large and widely spaced fractures where stress drop reaches the maximum magnitude ~3 MPa. Thus the energy release from these large (~200–1200 m) and closely spaced (~150 m) fractures within the reservoir generate a higher number of seismic events with higher magnitude. This analysis gives significant information about the rate of migration of a seismic event within the reservoir and how it changes over time. The number of seismic events decreases during production by increasing the fracture density either for small or large fracture spacing. This behavior is related to evolving rates of thermal and hydraulic transport. The following section separately examines the rate of hydraulic and thermal transport within these reservoirs during long-term production.

5. Hydrodynamic and thermal front triggering of seismicity

This section discusses the mechanisms of seismic triggering by correlating the evolution of seismicity with the transit of the hydrodynamic and thermal fronts within the reservoir. The evolution of the seismicity from stimulation to production of a reservoir in the long term (i.e. 20 years) is illustrated by determining the propagation of fluid pressure and thermal fronts through the reservoir over time. Large magnitude events (1.5–1.9) are observed during early transit of the fluid pressure front transitioning to lower magnitude late-time events resulting from the secondary transit of the thermal front. Both temperature and pressure-diffusion may induce seismicity and may be related in a natural way to the triggering front concept (Shapiro and Dinske, 2007).

The hydrodynamic and thermal fronts are tracked as they propagate through the reservoir for various fracture networks of low to high density and at low and high initial stresses (shallow to deep zones). The location of these fronts is defined by the propagation of the fluid flow rate at any given time. The evolution of seismicity for long-term production (20 years) is shown in a radius-time plot relative to the propagation of the fluid and thermal fronts in Figs. 8 and 9 (injection flow rate is set at 44 *l/s* in the simulation). The figures show the progress of the fluid and thermal fronts in the reservoir, together with the progress of induced seismicity in both zones B and D with closely spaced (~150 m) and widely spaced (~300 m) fractures.

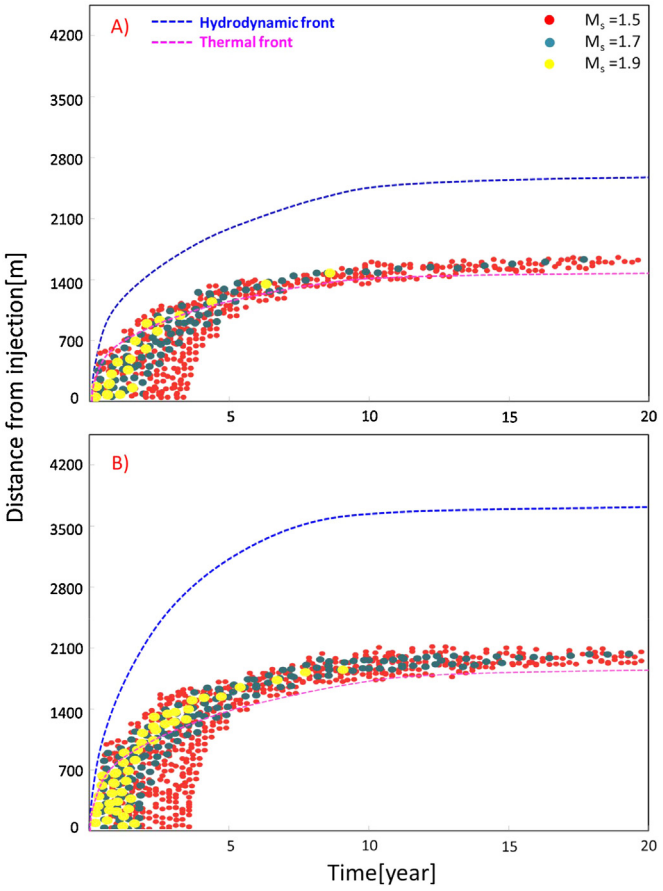

Fig. 8. Radius versus time plot for short term of the progress of fluid and thermal fronts in the reservoir and of induced seismicity (injection flow rate is 44 l/s). Reservoir located at two different zones (shallow to deep) and at two different depths of 2000 and 2750 after 20 years of reservoir production. The same network of large fractures (density of $0.003\,m^{-1}$ and spacing 300 m) applied at each zone. Larger seismic moment of individual events shown red: $M_s = 1.5$, blue: $M_s = 1.7$, yellow: $M_s = 1.9$. (A) For smaller fracture (10–200 m) the densities of $0.5\,m^{-1}$ in the shallow zone B. (B) Fracture density of $0.9\,m^{-1}$applied in the deeper zone D. (For interpretation of the references to color in this figure legend, the reader is referred to the web version of the article.)

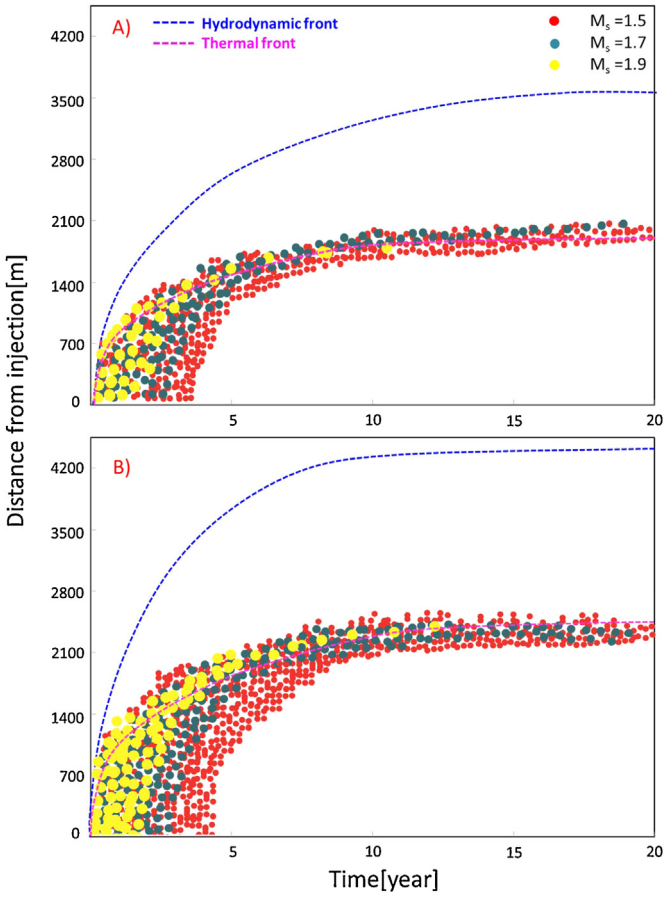

Fig. 9. Radius versus time plot for short term of the progress of fluid and thermal fronts in the reservoir and of induced seismicity (injection flow rate is 44 l/s). Reservoir located at two different zones (shallow to deep) and at two different depths of 2000 and 2750 after 20 years of reservoir production. The same network of large fractures (density of 0.006 m^{-1} and spacing 150 m) applied at each zone. Larger seismic moment of individual events shown red: M_s = 1.5, blue: M_s = 1.7, yellow: M_s = 1.9. (A) For smaller fracture (10–200 m) the densities of 0.5 m^{-1} in the shallow zone B. (B) Fracture density of 0.9 m^{-1} applied in the deeper zone D. (For interpretation of the references to color in this figure legend, the reader is referred to the web version of the article.)

Figs. 8 and 9 also show the progress of the fluid and thermal fronts in the reservoir, together with the progress of induced seismicity. The advancement rates of the hydraulic and thermal fronts as functions of the different fracture characteristics are observed first with a fracture network density of 0.5 m^{-1} in shallow zone B (Fig. 8A) and then with a density of 0.9 m^{-1} in deep zone D (Fig. 8B), followed by an observation of both with the same large fracture spacing of ~300 m. Further observations are made with a fracture network density of 0.5 m^{-1} in the shallow zone B (Fig. 9A). A density of 0.9 m^{-1} in the deep zone D (Fig. 9B) is used with the same small fracture spacing of ~150 m in both zones.

The deepest penetration of the hydrodynamic front into the reservoir at any given time is recorded for the network with the most closely spaced fractures (~150) (i.e. with the larger fracture density (0.9 m^{-1})) and for zone D at a deeper depth (2750 m) (Fig. 9B). This increased penetration could result from the larger permeability change for the more closely spaced network due to the immediate increase in fluid pressure as well as a drop in effective stresses. In addition, heat removal from the reservoir blocks are fastest for the most closely spaced fractures due to the (thermally) diffusive length scale defined by fracture spacing (Elsworth, 1989; Elsworth and Xiang, 1989).

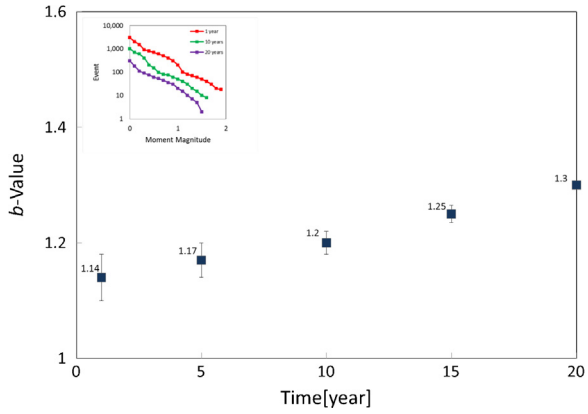

Fig. 10. Number of events as a function of magnitude indicating *b*-value for moment magnitudes in the range 0–1.3 after 20 years of reservoir production. Reservoir located in shallow zone D and at depth of 2750 m. *b*-values are evaluated at different times of production for the network of large fractures (density of 0.003 m^{-1} and spacing 300 m), and for the smaller fractures (10–200 m) with the density of 0.9 m^{-1}.

Events are separated into three magnitude classifications (M_S ~1.5, 1.7 and 1.9). It is observed that the number of seismic events decays with time and distance from the injection point for each reservoir. This illustrates that most of the seismic activity is triggered by hydraulic effects at early times (days to month) relative to the initiation of stimulation. At a later time (months to years later), thermal effects (and possibly chemical effects) may contribute to the seismicity when the seismicity front lags behind the hydrodynamic front.

6. Empirical relation for seismicity occurrence during production

The cumulative number of seismic events can be expressed by the magnitude distribution (Gutenberg and Richter, 1944) in the form $\log N_{event} = a - bM$, where N_{event} is the number of seismic events within a magnitude interval $M \pm \Delta M$. Here, a and b are constants that describe the productivity and the relative size distribution of the events, respectively.

This section discusses the scaling of event frequency, with N_{event} as a function of fluid pressure and temperature during reservoir production. The number of events as a function of time is controlled only by the cumulative mass of fluid injected, which can cause failure and result in energy release. The greater this energy release, the larger the number of events induced at a given location, and consequently the greater the probability of large-magnitude events. Thus, the model above is able to predict magnitude-frequency distributions.

The modeled *b*-value for the Newberry EGS at deeper zone D (0.9 m^{-1}) is illustrated in Figs. 10 and 11. Fig. 10 corresponds to the network with larger fracture spacing (~300 m), and Fig. 11 is related to smaller fracture spacing (~150 m).

By modeling results during stimulation (Izadi and Elsworth, 2014), it can be observed that the closely spaced fracture network with a higher stress regime (at the deeper level) has the largest *b*-value. This shows a greater number of events induced due to the existence of a higher density fracture network (0.9 m^{-1}) under the prescribed conditions of higher in situ stresses compared to the lower predicted *b*-value in the shallow zone with the lower density fracture network (Izadi and Elsworth, 2014). As a result, this section only considers the reservoir at the deeper level (zone D) when analyzing the change in the *b*-value during reservoir production. The main focus of this study is comparing the number of large

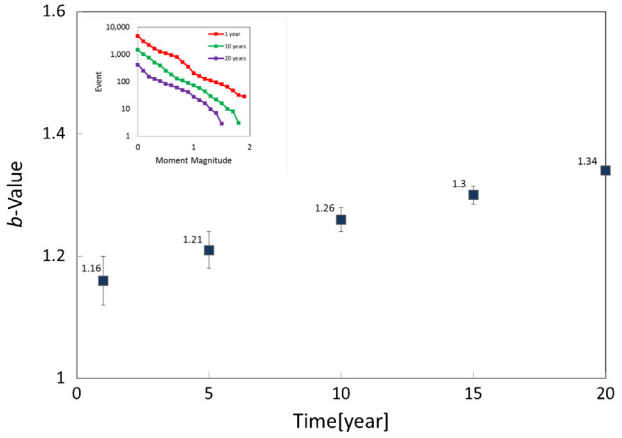

Fig. 11. Number of events as a function of magnitude indicating *b*-value for moment magnitudes in the range 0–1.34 after 20 years of reservoir production. Reservoir located in shallow zone D and at depth of 2750 m. *b*-values are evaluated at different times of production for the network of large fractures (density of 0.006 m^{-1} and spacing 150 m), and for the smaller fractures (10–200 m) with the density of 0.9 m^{-1}.

and small seismic events associated with large and small fracture spacing when the reservoir is located at the deeper zone (D).

The largest *b*-value (~1.34) is observed during production when the reservoir is seeded with closely-spaced fractures (150 m). These observations indicate that smaller fracture spacing results in both a higher *b*-value and a greater number of events; it is the dominant parameter influencing behavior.

Over longer periods of time (20 years), the largest *b*-value for the small and large fracture spacing shows more small events than large events during long-term production. The *b*-value varies from 1.14 to 1.30 for widely (300 m) spaced fractures and 1.16 to 1.34 for closely (150 m) spaced fractures in zone D. In both cases, the *a*-value decreases and the *b*-value increases – indicating both decreased magnitude and decreased number of events during long-term production when compared with those occurring during stimulation.

7. Thermal energy

The thermal output of the reservoir is examined after 20 years of production to consider the key influence of stress state and fracture network structure on thermal production. In this circumstance, the reservoir comprises fractures with either low or high fracture density and from shallow depth (zone B) to greater depth (zone D). These models examine the sensitivity of the network with large and small fracture spacing on thermal recovery within the reservoir during long-term reservoir production.

The rate of thermal energy production is a function of the fluid mass production rate and the temperature difference between the injected and recovered fluid. The thermal energy ($E_{thermal}$) recovered from the geothermal reservoir is defined as

$$E_{thermal} = \dot{M} c \Delta T \quad (3)$$

where mass flow rate is $\dot{M} = \rho, Q$, ρ is water density, Q is flow rate, and c is the specific heat capacity of the fluid. The temperature difference is $\Delta T = T_{production} - T_{injection\ fluid}$, where $T_{injection}$ is the injection fluid temperature and $T_{production}$ is the production temperature. The parameters used in the simulation are listed in Table 2. The estimated thermal energy for zones B and D, with small and large fracture spacing, is illustrated in Fig. 12C. The geometry of the reservoir for all zones is the same when the injector and producer are separated by 700 m.

The flow rate and temperature profile for both shallow to deep zones (B and D) is displayed in Fig. 12A and B. The highest flow rate is observed in systems where the smallest fracture spacing

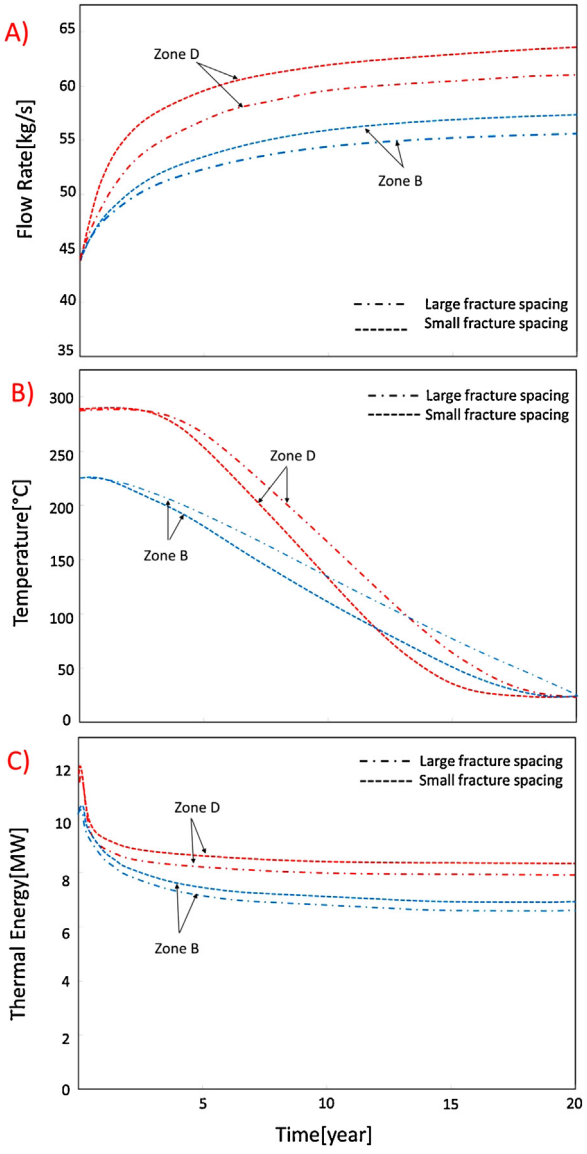

Fig. 12. Flow rate, temperature and thermal output for Newberry EGS after 20 years of production at two different depths of 2000 m and 2750 m. Blue dash lines relate to the network of closely and widely spaced fractures (~150 and 300 m) at shallow zone B, and red dash lines relate to the network of closely and widely spaced fractures (~150 and 300 m) at deeper zone D. (A) Flow rate profile. (B) Temperature profile. (C) Thermal recovery. (For interpretation of the references to color in this figure legend, the reader is referred to the web version of the article.)

(150 m) and highest fracture density network (0.9 m^{-1}) is applied. Because flow rate is a function of permeability changes as well as fracture surface area for closely spaced fractures (~150 m) with higher fracture density (0.9 m^{-1}), the migration of fluid pressures and thermal removal from blocks is much faster than for a network of widely spaced fractures (~300 m).

A previous study (Izadi and Elsworth, 2014) illustrated that the fluid penetration in a closely spaced network (zone D) is both larger and reaches further from the injection well when compared to the wider-spaced network (zone B). Thus the increased penetration of fluid injection results in a larger initial permeability change for the more closely spaced network. The higher density network (deep zone) with a closely spaced fracture can provide a larger permeable network and lead to increased flow rates (Fig. 12A). These results illustrate that if the fracture density is increased then such a system is capable of supporting much higher flow rates, which is also beneficial for higher rates of energy recovery. Thus flow rate in

the system is related to the fracture spacing and fracture density, which ultimately leads to decreased flow rates at increased fracture spacing.

Larger fracture density also increases the heat transfer area, which would significantly increase the performance of the system at an earlier time (~1 year). Higher rates of temperature decline when the zone is filled with a higher number of fractures, leading to more rapid advancement of the thermal front (Fig. 12B). By increasing the fracture spacing in shallow to deep zones, heat removal is slower compared to those with smaller fracture spacing. Such behavior illustrates that temperatures are able to change significantly during a long-term production period. This response will be fastest for the most closely spaced fractures due to the (thermally) diffusive length scale defined by fracture spacing (Elsworth, 1989; Elsworth and Xiang, 1989). Thus, for a deeper reservoir with smaller fracture spacing (~150 m), the cooling rate is fastest and the thermal transfer rate is highest.

As discussed, the more desirable system for energy recovery is achieved at early times (~1 year) when the fracture density is high and fracture spacing is small. Such a system is capable of supporting a thermal recovery close to ~10 MW in zone D and ~8 MW at zone B. The total thermal output of zones B, C, D and E is close to ~36 MW or ~14MWe for a conversion efficiency of 40%.

8. Conclusion

Using different experimental models, this paper examines the dominant behaviors influencing induced seismicity as well as heat production within EGS reservoirs during long-term production (~20 years). A THMC model is used to explore the roles of thermal-hydraulic-mechanical- and chemical-effects on different fractured reservoirs. Various fracture networks (low to high density) are considered for both closely and widely spaced fractures, and reservoir conditions change due to varying reservoir depths, shallow (2000 m) to deep (2750 m). These numerical models are applied to the Newberry EGS field (USA) to determine the effect of these key factors on induced seismicity during long-term (~20 years) reservoir production.

The results demonstrate that when a reservoir is located at greater depth and with more closely-spaced fractures (~150 m), the increase of fluid circulation is higher. The permeability change is propagated further from injection and occurs in a shorter time compared to those with a widely spaced fracture network (~300 m). Likewise, for the reservoir with the highest density of fractures and high initial stresses (due to greater depth) – the evolution of seismicity is more rapid (higher event rate), and its distribution expands faster with radius (zone D).

A maximum event magnitude for identical fracture distributions is $M_S \sim 1.9$, a magnitude directly related to the largest fracture size (~1200 m) and maximum prescribed shear stress drop (~3 MPa) in the reservoir.

The hydrodynamic and thermal fronts are also defined for different fracture structure (with closely-widely spaced fractures) to determine seismicity triggering during long-term production. A higher migration rate and a quicker advancement of these fronts is observed when the zone is filled with closely spaced fractures (~150 m) under the prescribed conditions of higher in situ stresses (deeper zone). As a result, larger numbers of seismic events are created due to higher flow rates when the fracture spacing is smallest.

There is a significant increase in both the number and magnitude of seismic events when the fracture density increases and fracture spacing decreases. The effects of thermal stress and pore pressure on the evolution of seismicity in reservoirs is examined separately and indicates that the most important mechanism triggering slip and promoting both the number of seismic events and the moment magnitude, is the augmentation of fluid pressure. The penetration of the hydrodynamic front is observed to be controlled principally by the size, number, location, and spacing of fractures.

When the spacing of fractures in the system is decreased, the fluid flow is able to penetrate more rapidly during injection.

We observe the propagation of fluid pressure and thermal fronts generate seismic events thorough reservoir with time. Large events at early-time (days to month) occurs due to the fluid front. Over longer periods of time (month to years) smaller seismic magnitude formed as a result of thermal (-chemical) front within reservoir.

The network with small (~150 m) fracture spacing is capable of generating the highest flow rate and as a result is the fastest propagating hydrodynamic front observed. This behavior allows the system to create a large number of events with highest magnitude (1.9) from months to years after the start of injection.

We then modeled the *b*-value for different fracture networks with different fracture spacing (the *b*-value describes the fracture process within reservoirs and is related to the size, location, distribution, and spacing of fractures) and characterized the induced seismicity by the *b*-value for shallow (B) to deep zones (D). The largest *b*-value was observed at zone D, indicating a larger number of triggered seismic events (also with a larger distribution in location). The approximate *b*-value for the Newberry EGS in the deepest zone (D) for two different fracture spacing shows that the smaller fracture spacing (~150 m) has the highest *b*-value. The *b*-value regime in small and large fracture spacing indicates a higher number of events when the spacing is decreased.

The temperature and flow rate profile for shallow and deep zones B and D with small and large fracture spacing was examined to evaluate the thermal recovery from these zones after 20 years of reservoir production. The highest thermal output is from the deeper zone D with a closely spaced fracture network. A high number of fractures in the system with small spacing between fractures increases the rate of cooling and contributes to having a quicker decline in temperature and also to generating a fluid flow path for a higher system flow rate. Based on the information discussed above, this paper concludes that the total thermal output for Newberry EGS at four shallow to deep zones B, C, D and E is close to ~36 MW or ~14 MWe.

Acknowledgements

This work is a partial result of support from the Department of Energy Office of Energy Efficiency and Renewable Energy and Geothermal Technology Program under contract EE-10EE0002761. This support is gratefully acknowledged. We also appreciate a final professional edit by Susan J. Burlingame.

References

Aki, K., 1967. Scaling law of seismic spectrums. J. Geophys. Res. 72, 1217–1231.

Audigane, P., Royer, J., Kaieda, H., 2002. Permeability characterization of the Soultz and Ogachi large-scale reservoir using induced microseismicity. Geophysics 67, 204–211.

Baisch, S., 2009. Deep Heat Mining Basel – Seismic Risk Analysis, Technical Report. Serianex, Bad Bergzabern, Germany.

Cladouhos, T., Petty, S.C., Osborn, W., Hickman, S., Davatzes, N., 2011. The role of stress modelling in stimulation planning at the Newberry volcano EGS demonstration project. In: Thirty-Sixth Workshop on Geothermal Reservoir Engineering, Stanford, CA.

Deichmann, N., Giardini, D., 2009. Earthquakes induced by the stimulation of an enhanced geothermal system below Basel (Switzerland). Seismol. Res. Lett. 80 (5), 784–798.

Delépine, N., Cuenot, N., Rothert, E., Parotidis, M., Rentsch, S., Shapiro, S., 2004. Characterization of fluid transport properties of the Hot Dry Rock reservoir Soultz-2000 using induced microseismicity. J. Geophys. Eng. 1 (1), 77–83.

Dinske, C., Shapiro, S., Häring, M., 2010. Interpretation of microseismicity induced by time-dependent injection pressure. SEG Expand. Abstr. 29, 2125, http://dx.doi.org/10.1190/1.3513264.

Elsworth, D., 1989. Theory of thermal recovery from a spherically stimulated HDR reservoir. J. Geophys. Res. 94 (B2), 1927–1934.
Elsworth, D., Xiang, J., 1989. A reduced degree of freedom model for permeability enhancement in blocky rock. Geothermics 18 (5/6), 691–709.
Evans, K., Moriya, H., Niitsuma, H., Jones, R., Phillips, W., Genter, A., Sausse, J., Jung, R., Baria, R., 2005. Microseismicity and permeability enhancement of hydrogeologic structures during massive fluid injections into granite at 3 km depth at the Soultz HDR site. Geophys. J. Int. 160 (1), 388–412, http://dx.doi.org/10.1111/j.1365-246X.2004.02474.x.
Goodman, 1976a. Methods of Geological Engineering in Discontinuous Rocks. West Publishing, New York.
Goodman, 1976b. Methods of Geological Engineering in Discontinuous Rocks. West Publishing, New York, pp. 472.
Gutenberg, B., Richter, C.F., 1944. Frequency of earthquakes in California. Bulletin of the Seismological Society of America 34, 185–188.
Izadi, G., Elsworth, D., 2014. Reservoir stimulation and induced seismicity: roles of fluid pressure and thermal transients on reactivated fractured networks. Geothermics 51, 368–379.
Izadi, G., Elsworth, D., 2013. The effects of thermal stress and fluid pressure on induced seismicity during stimulation to production within fractured reservoirs. Terra Nova 25 (5), 374–380, http://dx.doi.org/10.1111/ter.12046.
Jaeger, J.C., Cook, W.G.W., Zimmerman, R.W., 2007. Fundamentals of Rock Mechanics. In: Fourth Edition. Blackwell Publishing, Malden, MA, pp. 475.
Jung, R., Cornet, F., Rummel, F., Willis-Richard, J., 1996. Hydraulic stimulation results 1992/1993. In: Baria, R., Baumgärtner, J., Gérard, A. (Eds.), European Hot Dry Rock programme 1992-1995: Extended Summary of the Final Report to the European Community (DG XII), pp. 31–41, Contract N JOU2-CT92-0115.
Kanamori, H., 1977. The energy release in great earthquakes. Geophys. Res. 82, 2981–2987.
Keylis-Borok, V.I., 1959. On estimation of the displace-ment in an earthquake source and of source dimensions. Ann. Geofis. 12, 205–214.
Polak, A., Elsworth, D., Yasuhara, H., et al., 2003. Permeability reduction of a natural fracture under net dissolution by hydrothermal fluids. Geophys. Res. Lett. 30 (20), http://dx.doi.org/10.1029/2003GL017575.
Purcaru, G., Berckemer, H., 1978. A magnitude scale for very large earthquakes. Tectonophysics 49, 189–198.
Renshaw, C.E., 1995. On the relationship between mechanical and hydraulic apertures in rough-walled fractures. J. Geophys. Res. 100, 24629–24636.
Rothert, E., Shapiro, S.A., 2003. Microseismic monitoring of borehole fluid injections: data modeling and inversion for hydraulic properties of rocks. Geophysics 68 (2), 685–689, http://dx.doi.org/10.1190/1.1567239.
Rutledge, J.T., Phillips, W.S., 2003. Hydraulic stimulation of natural fractures as revealed by induced microearthquakes, Carthage Cotton Valley gas field, east Texas. Geophysics 68, 441–452.
Rutqvist, J., Wu, Y.S., Tsang, C.F., Bodvarsson, G., 2001. A modeling approach for analysis of coupled multiphase fluid flow, heat transfer, and deformation in fractured porous rock. Int. J. Rock Mech. Miner. Sci. (submitted for publication).
Shapiro, S.A., Dinske, C., 2007. Violation of the Kaiser effect by hydraulic-fracturing-related microseismicity. J. Geophys. Eng. 4, 378–383.
Shapiro, S.A., Royer, J.J., Audigane, P., 1998. Estimating the permeability from fluidinjection induced seismic emission. In: Thimus, J.-F., Abousleiman, Y., Cheng, A.H.-D., Coussy, O., Detournay, E. (Eds.), Poromechanics. Balkema, Rotterdam, pp. 301–305.
Shapiro, S.A., Rothert, E., Rath, V., Rindschwentner, J., 2002. Characterization of fluid transport properties of reservoirs using induced microseismicity. Geophysics 67, 212–220.
Taron, J., Elsworth, D., 2009. Thermal–hydrologic–mechanical–chemical processes in the evolution of engineered geothermal reservoirs. Int. J. Rock Mech. Min. Sci., http://dx.doi.org/10.1016/j.ijrmms.2009.01.007.
Taron, J., Elsworth, D., Min, K.-B., 2009a. Numerical simulation of thermal–hydrologic–mechanical–chemical processes in deformable, fractured porous media. Int. J. Rock Mech. Min. Sci., http://dx.doi.org/10.1016/j.ijrmms.2009.1001.1008.
Taron, J., Elsworth, D., Min, K.B., 2009b. Numerical simulation of thermal–hydrologic–mechanical–chemical processes in deformable, fractured porous media. Int. J. Rock Mech. Min. Sci. 46 (5), 842–854.
Yasuhara, H., Elsworth, D., Polak, A., 2004. Evolution of permeability in a natural fracture: significant role of pressure solution. J. Geophys. Res. 109 (B03204), http://dx.doi.org/10.1029/2003JB002663.
Yeo, I.W., De Freitas, M.H., Zimmerman, R.W., 1998. Effect of shear displacement on the aperture and permeability of a rock fracture. Int. J. Rock Mech. Min. Sci. 35 (8), 1051–1070.
Zoback, M., Harjes, H.P., 1997. Injection induced earthquakes and the crustal stress at 9 km depth at the KTB deep drilling site, Germany. J. Geophys. Res. 102, 18477–18492.